Rothamsted Repository Download

A - Papers appearing in refereed journals

Holman, F. H., Riche, A. B., Castle, M., Wooster, M. J. and Hawkesford, M. J. 2019. Radiometric calibration of 'Commercial off the shelf' cameras for UAV-based high-resolution temporal phenotyping of reflectance and NDVI. *Remote Sensing.* 11 (14), p. 1657.

The publisher's version can be accessed at:

- https://dx.doi.org/10.3390/rs11141657
- https://www.mdpi.com/2072-4292/11/14/1657

The output can be accessed at: https://repository.rothamsted.ac.uk/item/8wx1q.

Radiometric calibration of 'Commercial off the shelf' cameras for UAV-based high-resolution temporal phenotyping of reflectance and NDVI.

Fenner H. Holman[1] *, March Castle[2], Andrew B. Riche[2], Martin J. Wooster[1,3], Malcolm J. Hawkesford[2]

[1] Department of Geography, King's College London, London WC2B 4BG; fenner.holman@kcl.ac.uk, martin.wooster@kcl.ac.uk.

[2] Rothamsted Research, Harpenden, Hertfordshire, AL5 2JQ; andrew.riche@rothamsted.ac.uk, malcolm.hawkesford@rothamsted.ac.uk, march.castle@rothamsted.ac.uk.

[3] National Centre for Earth Observation (NCEO), Leicester, LE1 7RH, UK.

* Correspondence: fenner.holman@kcl.ac.uk

Abstract: Vegetation indices, such as the Normalised Difference Vegetation Index (NDVI), are common metrics used for measuring traits of interest in crop phenotyping. However traditional measurements of these indices are often influenced by multiple confounding factors such as canopy cover and reflectance of underlying soil, visible in canopy gaps. Digital cameras mounted to Unmanned Aerial Vehicles offer the spatial resolution to investigate these confounding factors, however incomplete methods for radiometric calibration into reflectance units limits how the data can be applied to phenotyping. In this study, we assess the applicability of very high spatial resolution (1cm) UAV-based imagery taken with commercial off the shelf (COTS) digital cameras for both deriving calibrated reflectance imagery, and isolating vegetation canopy reflectance from that of the underlying soil. We present new methods for successfully normalising the imagery for exposure and solar irradiance effects, generating multispectral (RGB-NIR) orthomosaics of our target field based wheat crop trial. Validation against measurements from a ground spectrometer showed good results for reflectance ($R^2 \geq 0.6$) and NDVI ($R^2 \geq 0.88$). Application of imagery collected through the growing season and masked using the Excess Green Red index was used to assess the impact of canopy cover on NDVI measurements. Results showed the impact of canopy cover artificially reducing plot NDVI values in the early season, where canopy development is low.

Keywords: Unmanned Aerial Vehicle, reflectance, radiometric calibration, NDVI, digital cameras, canopy reflectance.

1. Introduction

In crop phenotyping, vegetation indices (e.g. NDVI) derived from canopy reflectance are commonly used to assess certain physiological traits of interest [1]; including (i) plant vigour [2,3], (ii) plant biomass [4,5], (iii) plant nitrogen status [6], (iv) plant Leaf Area Index (LAI) [7,8] and (v) final crop yield [9]. However, these indices are typically influenced by both the target vegetation condition and variables such as background soil properties and canopy cover/density [10]. The combined influence of each variable quite often remains unacknowledged when associating vegetation indices (VIs) to traits of interest; a problem when there are multiple situations (e.g. low canopy cover and high vegetation vigour *vs*. high canopy cover and low vegetation vigour) that may equate to similar VI measures. Such situations can provide significant uncertainty, and even false indications of plant status [11]. Traditional methods of measuring canopy spectral reflectance (e.g. ground spectrometers and/or satellite based remote sensing) offer insufficient spatial resolution to

investigate and dissect the influences of the many variables involved in controlling VI measures. Unmanned Aerial Vehicle (UAV) based remote sensing systems may, however, offer this capability, and are becoming a prominent method for high throughput phenotyping of field-based crop trials, largely thanks to their very high spatial resolution imagery [12].

In combination with modified digital cameras or commercially available multispectral imagers, low-cost UAVs are increasingly being used for high temporal resolution crop condition monitoring and field phenotyping. More recently modified single and dual 'commercial off the shelf' (COTS) digital camera systems are being used for collection of multispectral (RGB–NIR) imagery at spatial resolutions superior to those achieved by commercial cameras such as the Parrot Sequoia [13]. However, captured imagery is still subject to distortions from camera (exposure, vignetting, file format and spectral sensitivity), and environmental factors (predominantly solar spectral irradiance) [14–23], weakening the capacity to extract accurate quantitative information [15,24]. Whilst calibration methods for the bulk of these factors have been investigated, shortcomings remain in relation to long term consistency, particularly in relation to variable solar irradiance. Firstly, obtaining temporally relevant measures of irradiance for individual UAV images is a challenge. Berra et al. [25] used ground based artificial targets of known reflectance, along with the empirical line method, to convert camera measures to reflectance units. However, inconsistent capturing of targets within individual images limited calibration to final orthomosaics. Therefore variations in irradiance during the flight were not corrected for, increasing errors in the derived reflectance datasets [26]. Furthermore, the temporal stability of reflectance of such artificial targets left out in the field can vary by up to 16% over a season [27]. An alternative is to use a supplementary device measuring irradiance concurrently with COTS camera data collection, providing the information to convert individual images into reflectance units. The Parrot Sequoia employs this method, utilising its own downwelling light sensor operating at the same spectral bands as the imager itself. The second shortcoming identified relates to the fixing of exposure settings (aperture, shutter speed and ISO) to remove influence of camera exposure settings on the amount of light reaching the sensor, or the sensitivity of the sensor to light. This "fixed settings" approach increases risk of under or over exposure of images - which equates to lost data [28]. Linear relationships between image DN and varying ISO, shutter speed and aperture have been previously demonstrated [29], indicating post-capture normalising of images of varying exposure can be achieved. As far as we can tell this feature has not been utilised for this purpose before.

Given the above, the aim of the current study is to calibrate individual wavebands of dual COTS cameras to reflectance, with a focus to include individual image irradiance corrections from a separate irradiance sensor and allowance for non-fixing of camera exposure. Then, within a field phenotyping setting, using a low-cost UAV utilise the very high-resolution reflectance imagery to temporally analyse the influence of canopy structure and soil reflectance on derived vegetation indices, specifically NDVI. Within this framework, specific objectives are to:

1. Develop a method for full radiometric calibration of COTS camera imagery, with new methods for exposure normalisation and individual image incoming solar irradiance adjustment.
2. Quantitatively assess the influence of the radiometric calibration steps and the final quality of the derived reflectance and NDVI datasets.
3. Utilise the very high-resolution maps derived from the UAV imagery to analyse the influence of canopy cover on NDVI trends for a field based wheat crop trial.

2. Materials and Methods

2.1 Field Site

All data was collected at the experimental farm operated by Rothamsted Research, UK (51°48′34.56″N, 0°21′22.68″W). We focused on the Defra-funded Wheat Genetic Improvement Network (WGIN) Diversity Field Experiment [24], whose aim is to test the influence of applying different nitrogen fertiliser treatments to different wheat cultivars. A total of 30 different cultivars were grown at 4 different nitrogen application rates, with three replicates making a total of 360 plots. (Table 1) [25]. Each plot consisted of a 9m x 3m non-destructive plot and a 2.5m x 3m plot reserved for destructive sampling. This study focuses on the non-destructive part only.

Table 1. Details of the four nitrogen treatments applied to the diversity field experiment for 2017.

Treatment Code	Total Nitrogen Application (kg N ha^{-1})	Application Date	Nitrogen Applied (kg N ha^{-1})
N1	*0*	*-*	*0*
		-	*0*
		-	*0*
N2	*100*	*15/03/2017*	*50*
		05/04/2017	*50*
		09/05/2017	*0*
N3	*200*	*15/03/2017*	*50*
		05/04/2017	*100*
		09/05/2017	*50*
N4	*350*	*15/03/2017*	*50*
		05/04/2017	*250*
		09/05/2017	*50*

2.2 UAV Imagery

A DJI S900 UAV [30] fitted with a DJI flight controller was flown on a pre-determined flight plan at 45 m altitude over the field site nine times between 7th March 2017 and 4th July 2017. The flight plan was designed to ensure 80% overlap between concurrent images was obtained. Two Sony α5100 mirrorless digital cameras [31] mounted on the UAV were used for the image collection. These cameras contain 24.3 mega pixel complementary metal-oxide semiconductor (CMOS) sensors, and both were fitted with 20mm F2.8 Sony prime lenses. One camera was left as standard to record RGB imagery, and one had had its internal NIR-blocking filter replaced with an 830nm long pass filter to block visible light and enable recording of NIR waveband imagery. The 830nm filter was selected to ensure minimal capturing of visible light in the imagery, as seen with the 660nm filter used by Berra *et al.*[25,32]

All images were captured at 1-sec intervals and in RAW format, with focus set to 45 m to reflect the UAV flying height. Aperture and ISO were left on automatic, whilst shutter speed was fixed to 1/500sec to ensure minimisation of motion blur. The UAV and cameras were flown over the field site at a time relatively close to local solar noon, with actual recording times varying from 10:11 to 13.25. Twelve Ground Control Points, whose positions were measured with a Trimble Geo 7 DGPS [33], were used for georeferencing final orthomosaics. To provide measures of total incoming solar irradiance, a Tec5 HandySpec Field spectrometer [34] fitted with a cosine corrected downwelling optic was deployed at a fixed location next to the field and set to measure at 1-second intervals. Spectral measurements were collected at 10 nm spectral resolution across the wavelength range 360-1000 nm.

2.3 Validation Data

123   Mean plot canopy reflectance, measured with the Tec5 HandySpec Field spectrometer, were
124 used for validation of UAV derived canopy reflectance measures. To collect the spectrometer
125 measurements, a single scan of each plot's canopy was collected with the spectrometer optic held
126 approximately 1m above the plot; the standard procedure employed by Rothasmted Research. Each
127 scan produced one spectral reflectance measure for the plot at 10 nm spectral resolution across the
128 wavelength range 360-1000 nm. This procedure was repeated for all 360 plots on three separate dates
129 during the growing season between 19th April and 4th July 2017. The Tec5 HandySpec adjusts for
130 changes in solar illumination between measurements using a downwelling optic fitted with a cosine
131 diffuser; reflectance is calculated using proprietary software. Before comparing to UAV results, the
132 Tec5 results were convolved to the same spectral wavebands as the cameras. These ground-based
133 measurements were not always collected on the same days as UAV flights due to logistical
134 constraints, but were within 3 days. Additional validation data was obtained by flying a Parrot
135 Sequoia multispectral imager [13] simultaneously with the dual camera system for a single date (21st
136 June 2017). The Sequoia was set to capture images every second and the Sequoia's downwelling
137 sunshine sensor was mounted atop the UAV for collection of irradiance measurements. The Sequoia
138 images were processed using Pix4D (Version 4.3.1) [35] using standard recommended settings,
139 downwelling light sensor data and manufacturer derived calibrations, producing Green, Red, and
140 NIR reflectance orthomosaics at a ground sampling distance (GSD) of 5cm.
141   Due to the differences between COTS camera and Parrot Sequoia spectral responses (Table 2),
142 direct comparison between the cameras was not possible. Therefore, assessment of accuracy of the
143 individual UAV-based imaging systems was conducted by comparing both against the Tec5.

144

145   Table 2. Spectral sensitivities for the Parrot Sequoia's four spectral bands.

Camera Channel	Wavelength Range (nm)
Green	*530-570*
Red	*640-680*
Red Edge	*730-740*
NIR	*770-810*

146

147

148   *2.4 Post-processing of Captured Imagery*

149   The processing of the dual-camera imagery followed the workflow outlined in Figure 1.

150   Specific details on the main correction steps, including the novel exposure corrections are provided.
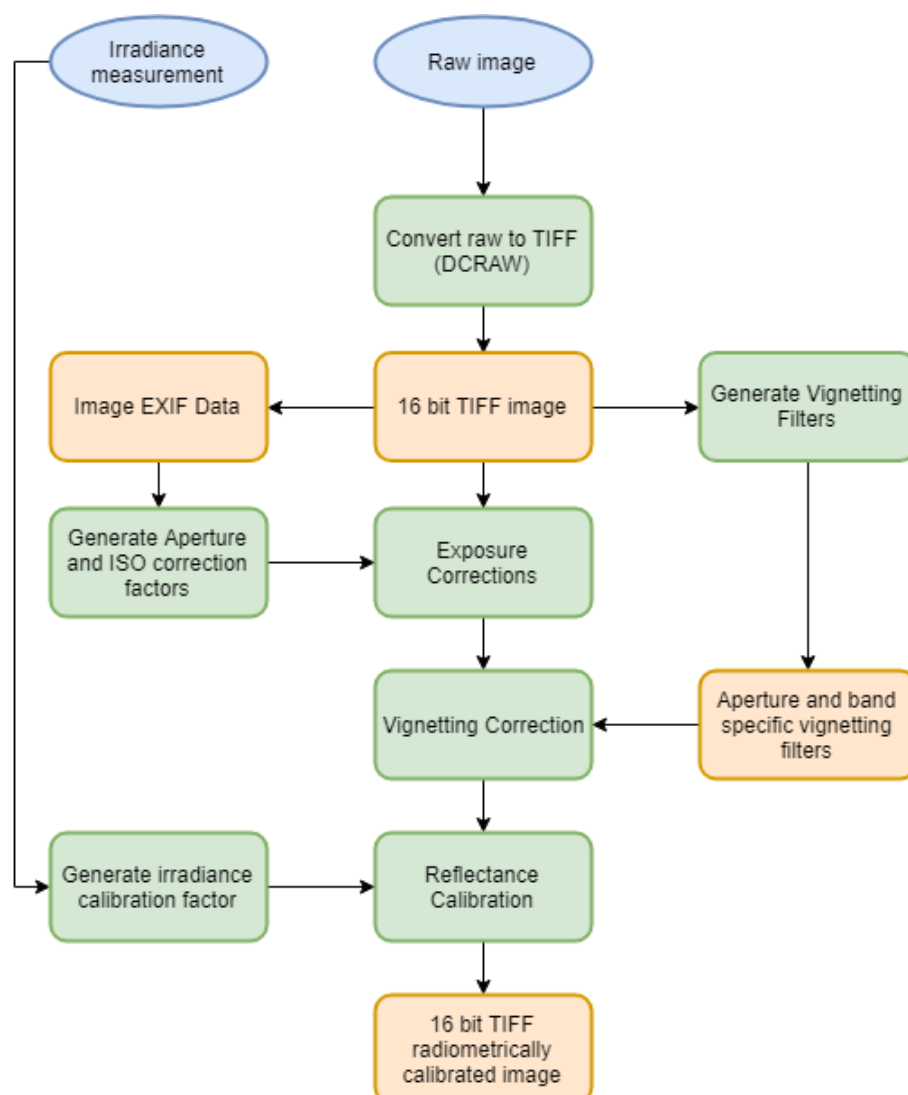
151

Figure 1. Flow chart of key processing steps used to convert raw images to reflectance images. The blue circles indicate inputs, green squares indicate processing steps and yellow squares derived products.

152 2.4.1 Relative Spectral Response

153   Relative Spectral Responses (RSR), Figure 2, of both cameras were determined using a double
154 monochromator fitted with an integrating sphere, using the method described by Berra *et al.* [32]. The
155 unmodified RGB camera shows greatest sensitivity in the green channel, as expected from a Bayer
156 matrix colour filter array [32]. For the modified NIR camera, overall sensitivity was similar in all three
157 bands that originally measured Red, Green and Blue waveband light. Whilst now mostly sensitive to
158 NIR wavelength light, all channels show some sensitivity to light below 830 nm (*i.e.* sensitivity to
159 radiation outside the NIR spectral range remained), indicating the modified internal filter was not
160 performing at 100% at 830nm. The 'Blue' channel of the NIR-adapted camera displayed the least
161 sensitivity to light below 830 nm, therefore was best suited for use as the NIR channel. The
162 wavebands determined for each channel of the RGB and NIR channels are presented in Table 3.
163
164   Table 3. Sony α5100 camera band sensitivities. Sensitivities were measured using a double
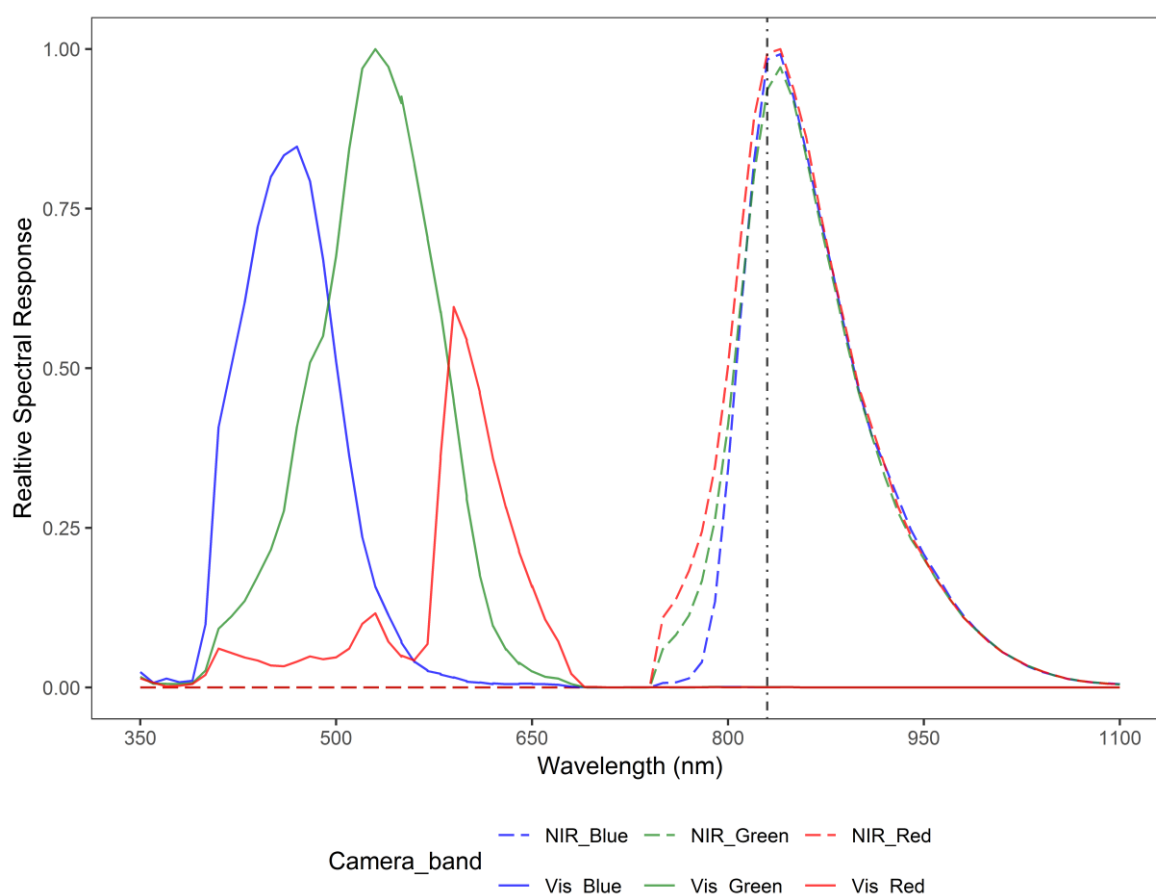

Figure 2. Relative Spectral response of the two Sony cameras used in this study. Vertical dotted line indicates the 830nm blocking filter present in the adapted Sony NIR camera.

165 monochromator fitted with an integrating sphere.

Model	Channel	Wavelength Range (nm)
"RGB" Camera	*Red*	*580-660*
	Green	*420-610*
	Blue	*410-540*
"NIR" Camera	*NIR (blue channel)*	*800-900*

166 2.4.2 RAW Conversion

167   Images were collected in RAW format before conversion to 16-bit TIFF format using DCRAW
168 9.27 [36]. This was done using bilinear conversion algorithms and a dark current correction, to
169 maintain original sensor DN measurements. The exact settings are presented in Table 4. Dark current
170 correction images for each camera were captured in complete darkness (*i.e.* lens cap on and lights
171 turned off), and used for the DCRAW processing.
172

173   Table 4. Details of DCRAW settings used to convert images from raw to TIFF.

DCRAW Command	Action
-v	*Print verbose messages*
-6	*Write 16bit*
-W	*No automatic image brightening*
-g 1 1	*Apply unadjusted gamma curve*
-T	*Write Tiff format*
-r 1 1 1 1	*Set unadjusted white balance*
-t 0	*Do not rotate image*
-q 0	*Apply linear demosaicing*
-o 0	*Raw output colour space*
-K darkimage.pgm	*Apply dark image correction using file specified*

174

175   2.4.3 Exposure Corrections

176   To determine the relationships between digital number and exposure settings (aperture and
177 ISO), a series of images were collected of a Lambertian spectralon reflectance panel, set up indoor
178 under constant illumination with white incandescent bulb light. For each exposure setting (aperture,
179 ISO and shutter speed), a series of images were captured under the settings full range (e.g. ISO100 –
180 ISO1000), whilst other settings remained fixed. As illumination remained constant; thee image sets
181 were produced, each modelling the influence of changing one exposure setting on image DNs.
182   Linear relationships between pixel DN and aperture and ISO were observed (Figure 3). From
183 these relationships, the aperture correction factor (CF$_{app}$) was derived to normalise images captured
184 under varied aperture to an aperture value of 1 (Equations 1 and 2).

$$Image_{app} = \frac{Image_{RAW}}{CF_{app}} \tag{1}$$

185   Where:

$$CF_{app} = \frac{1}{(fstop_{image})^2} \tag{2}$$

186
187   Where *f-stop* is the aperture value the image was captured with and *Image$_{RAW}$* is the DCRAW
188 converted TIFF image and *Image$_{app}$* is the aperture corrected image.
189   For ISO, Equation 3, was used to normalise images to an ISO value of 100, the lowest and most
190 commonly used setting on the cameras.

$$Image_{ISO} = \frac{Image_{app}}{\left(\frac{ISO_{image}}{100}\right)} \tag{3}$$

191 Where ISO_{image} is the ISO setting used to capture the image; $Image_{app}$ is the aperture corrected image;
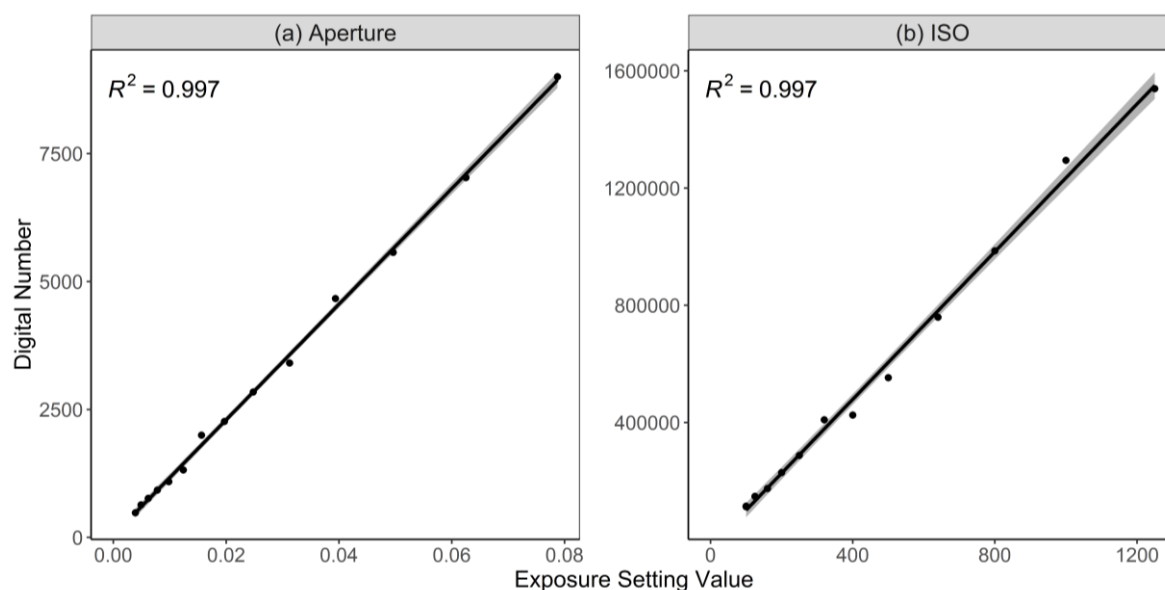192 and $Image_{iso}$ is the ISO and aperture corrected image.

Figure 3. Linear relationships and R^2 between camera exposure settings, (a) aperture and (b) ISO, and image digital numbers. For (a) Aperture, f-numbers have been converted from 'stops' to aperture diameter via $1/f\text{-stop}^2$.

193 2.4.4 Vignetting Correction

194 An adapted version of the method outlined by LeLong *et al.* [16] was used in this study; such
195 that camera, band and aperture specific vignetting correction filters were generated for each data
196 collection date. For each flight, the following steps were taken to produce vignetting filters:

1. Images of matching camera, band and aperture settings were summed together and averaged.
2. The radial vignetting profile of the averaged image was modelled using the median of evenly spaced concentric rings.
3. A 2nd degree polynomial function interpolated the vignetting profile from the median of rings.
4. The interpolation values were then divided by the minimum value to produce a multiplicative correction factor which brightened the corners.
5. The concentric rings are given the value of the correction factor corresponding to its distance from the centre to produce the final vignetting filter (Figure 4 middle).

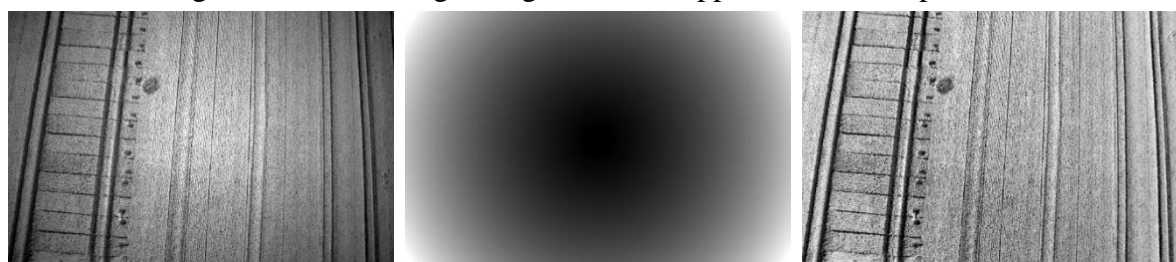207 Unlike LeLong *et al.*[16], the vignetting filter was applied as a multiplicative filter rather

Figure 4..Example of input NIR image (left), generated vignetting filter (middle) and vignetting corrected image (right).

208 than additive, this is in order to maintain the underlying patterns within the original
209 images.2.4.5 Cross Calibration Factor and Reflectance Calibration

210   Before converting image DNs to reflectance, it was necessary to cross calibrate the Tec5
211 downwelling sensor and the cameras. To do this the empirical line method was used to retrieve the
212 relationship between Tec5 irradiance measures and exposure and vignetting corrected image DN,
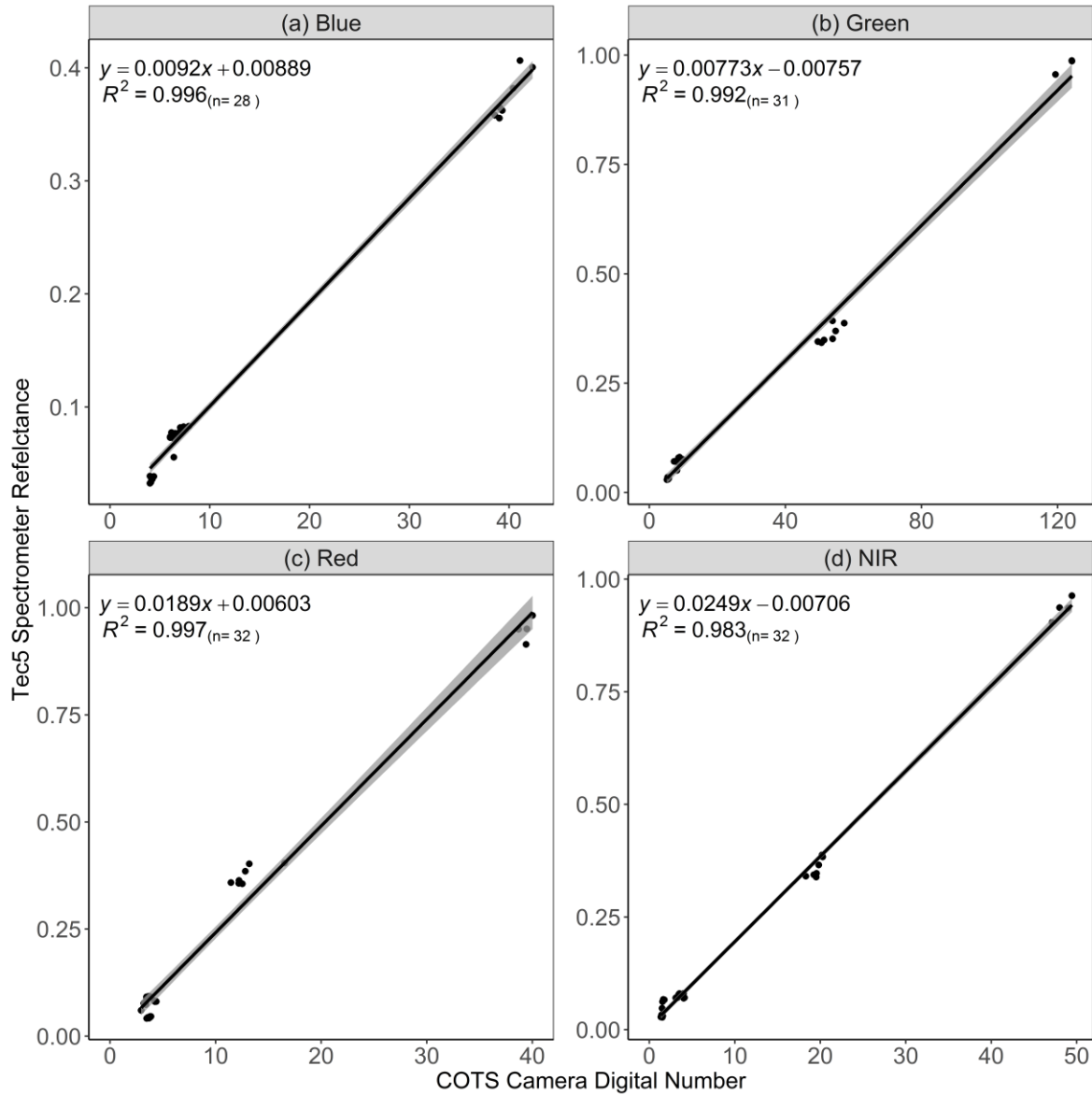213 over 5 Lambertian reference targets (Figure 5).

Figure 5. Results of relationships between exposure and vignetting corrected image DNs and Tec5
spectrometer reflectance. All camera bands show strong linear agreements with Tec5 reflectance.
Measurements of 5 black, grey and white spectral reflectance targets were used for this.

214   The camera and band specific calibration factors, Table 5, were applied to individual images,
215 before Equation 4 was used to convert images from DN to reflectance using time matched Tec5
216 irradiance measurements.
217

218   Table 5. Calibration equations for each of the four camera bands. Equations were derived from
219   comparison of camera and Tec5 measurements of 5 reference targets.

Camera and Band	Calibration Equation
RGB – Blue	$0.0092 \times DN + 0.00889$
RGB – Green	$0.00773 \times DN + 0.00757$
RGB – Red	$0.0189 \times DN + 0.00603$
NIR - Blue	$0.0249 \times DN - 0.00706$

220

$$R_{b,t} = \frac{Image_{b,t}}{Tec5\ irradiance_{b,t}} \qquad (4)$$

221   Where $R_{i,t}$ is the final reflectance image at time *t* and waveband *b*, $Image_{b,t}$ is the single image captured
222   at time *t* and band *b*, and Tec5 irradiance$_{b,t}$ is the Tec5 irradiance measurement captured at the same
223   time, *t* and convolved to the same band *b* as the image.

224   2.4.6 Orthomosaic Generation

225   Agisoft Photoscan (1.4.3) [37] was used to process final imagery to orthomosaics, including
226   automatic lens correction. For each date, two orthomosaics were generated, RGB and NIR. Agisoft
227   processing settings, Table 6 were kept consistent for all orthomosaics. In order to minimise the impact
228   of geometric distortion and variation, the disabled blending mode was used to generate the
229   orthomosaic [38]. This mode takes pixel data from the image whose view is closest to nadir.
230   Orthomosaics were generated and exported at 1cm Ground Sampling Distance (GSD).Table 6.
231   Processing settings for Agisoft Photoscan. The same settings were used for all Orthomosaics
232   generated.

Processing Step	Setting
Align Photos	*High*
Generate Dense Point Cloud	*Medium*
Generate Mesh	*High*
Generate Orthomosaic	*Disabled*

233

234   NDVI orthomosaics were generated using Equation 5, before mean values for each plot in each
235   camera band and NDVI were extracted using custom Python based processing tools. As in Holman
236   *et al.* [12], a 50cm buffer was applied to each plot before extracting mean values in order to prevent
237   influence of plot edge effect.

$$NDVI = \frac{R_{NIR} - R_r}{R_{NIR} + R_r} \qquad (5)$$

238
239   Where R_{NIR} is measured reflectance in the NIR band and R_r is measured reflectance in the red band.
240

241   *2.5 Canopy Masking*

242   To dissect green canopy from background variables, the Excess Green Red (ExGR) index was
243   used (Equation 6), with a threshold of > 0 to classify green vegetation [39,40]. Figure 6 shows an
244   example of the produced mask, with reasonable agreement between visual green canopy and pixels
245   classified as green by ExGR. The masks were used to extract mean plot NDVI of green pixels only.
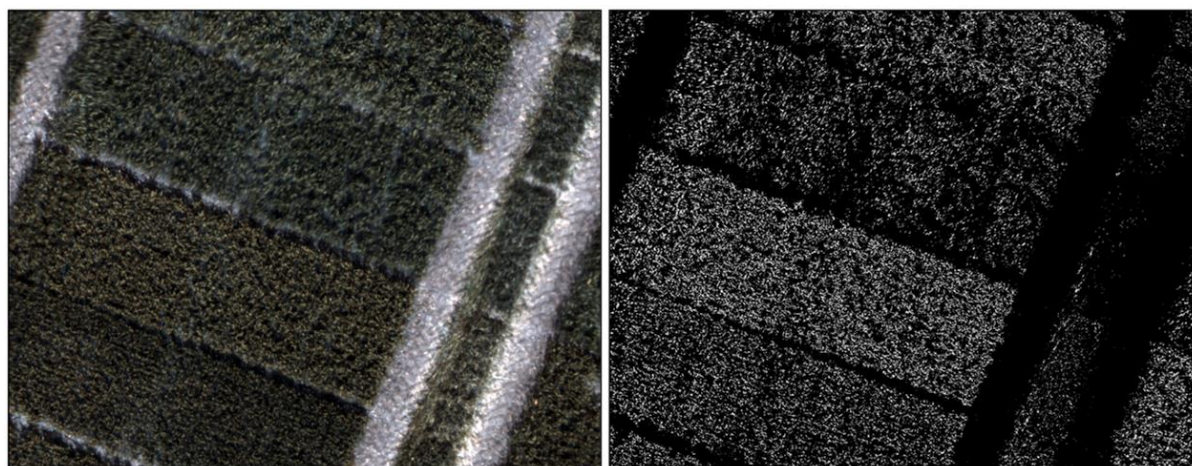
$$ExGR = (2 \times G - R - B) - (1.4 \times R - G) \tag{6}$$

Figure 6. Example image of an RGB image of wheat trial plots and right the ExGR mask output. In the ExGR mask white represents green classified pixels and black non-green pixels. Imagery is from the 21st June 2017 UAV data collection campaign.

246   **3. Results**

247   *3.1 Validation of Calibrations*

248   The influence of the calibration steps applied to COTS camera imagery on precision of results
249   was first assessed. For a single date (21st June 2017), camera imagery was processed with corrections
250   applied cumulatively to understand their influence on results. For clarity, extracted mean plot results
251   for the red and NIR bands have been scaled to a range 0-1.
252   Red band results (Figure 7) show little impact on linear trend and intercept from correction steps,
253   with consistent slopes around 1.2 and intercepts of 0.07. Correlations show improvement with
254   addition of corrections, R^2_{RAW} = 0.82 up to $R^2_{Vignetting}$ = 0.89, with camera related exposure and
255   vignetting offer the greatest gains. No meaningful effect on nRMSE and bias is gained from
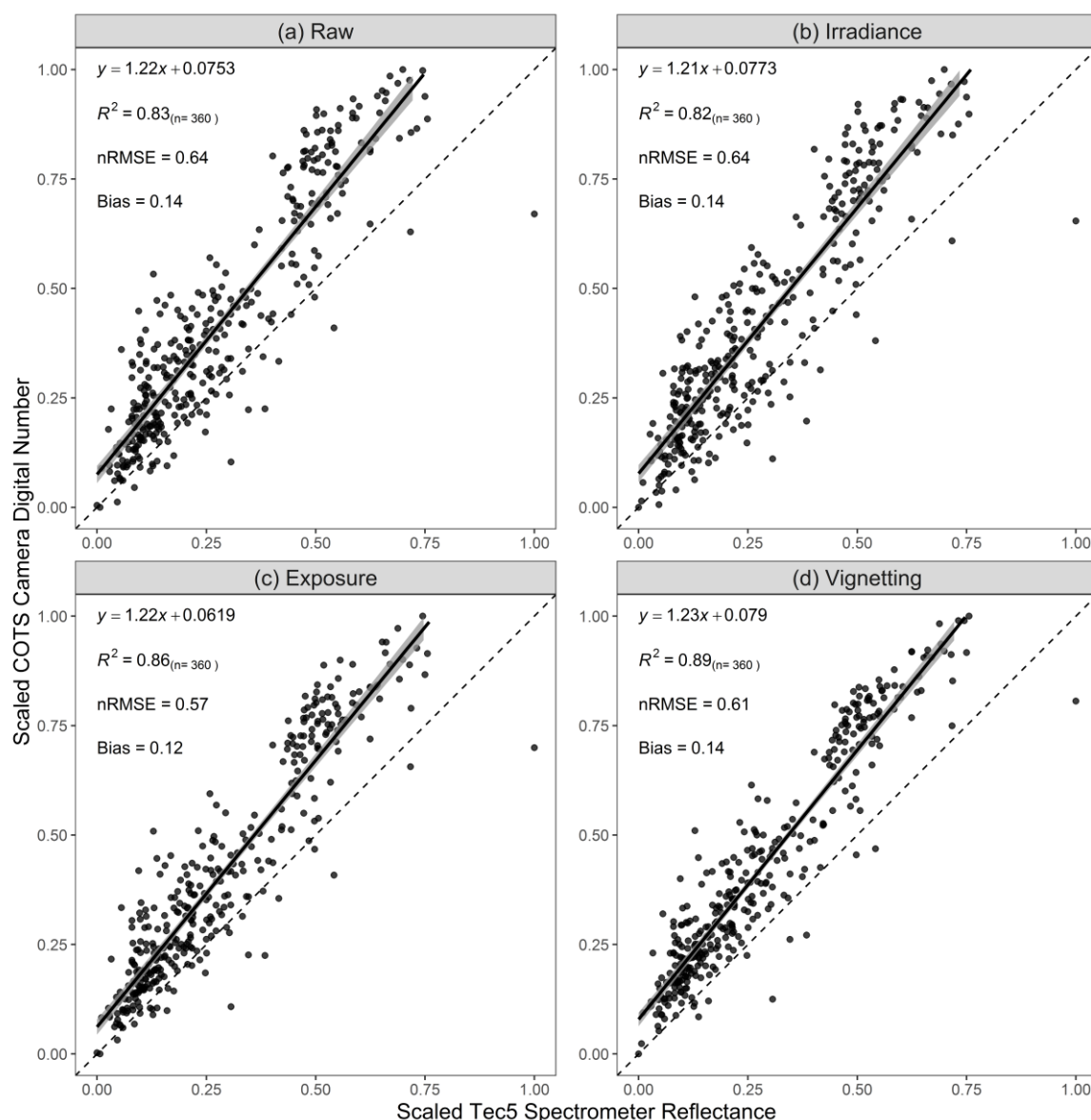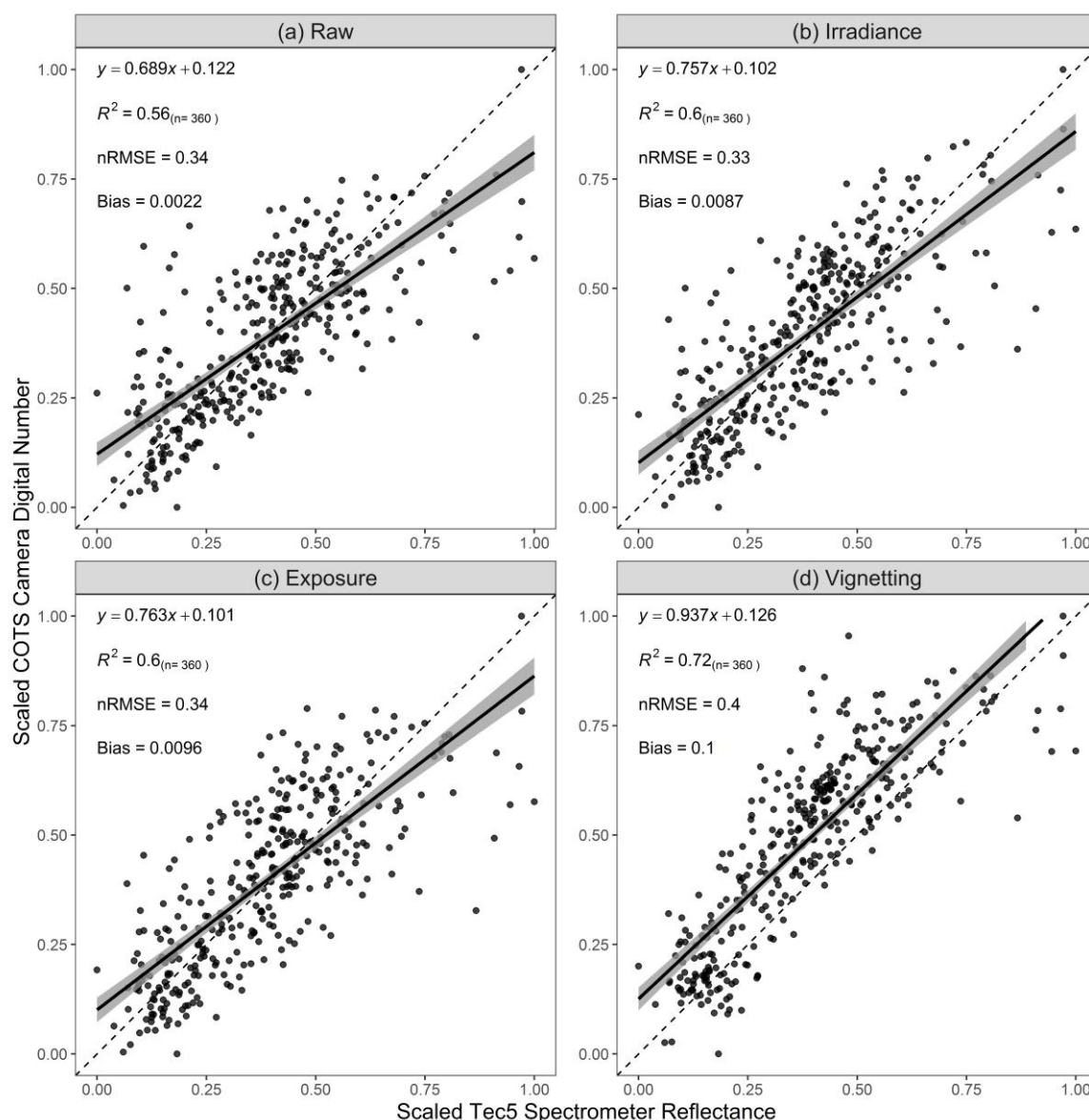256   corrections.

Figure 7. Assessment of the cumulative influence of correction steps on precision of scaled mean plot measurements in the red band. Results are compared to scaled COTS camera convolved Tec5 measurements of mean plot reflectance. The dashed line represents the 1:1 line.

For the NIR band (Figure 8), more significant impact of correction steps is observed. Gains in both the linear fit and R^2 are achieved at each step, with vignetting indicating most significant influence. Both nRMSE and bias decline in accuracy with the addition of correction steps.

Figure 8. Assessment of the cumulative influence of correction steps on precision of scaled mean plot measurements in the NIR band. Results are compared to scaled COTS camera convolved Tec5 measurements of mean plot reflectance. The dashed line represents the 1:1 line.

272   The influence of corrections on NDVI, calculated from non-scaled data (Figure 9), indicates high
273   precision ($R^2 = 0.91$) but poor accuracy (nRMSE = 0.85, Bias = -0.57) compared to the ground validation
274   data. Addition of irradiance correction greatly improves accuracy; particularly nRMSE, bias and
275   linear trend. Exposure corrections improve correlation, though drops in nRMSE and bias are also
276   introduced. Finally, the addition of vignetting improves all statistics, indicating the complete
277   collection of calibration steps produces best results in terms of both accuracy and precision.
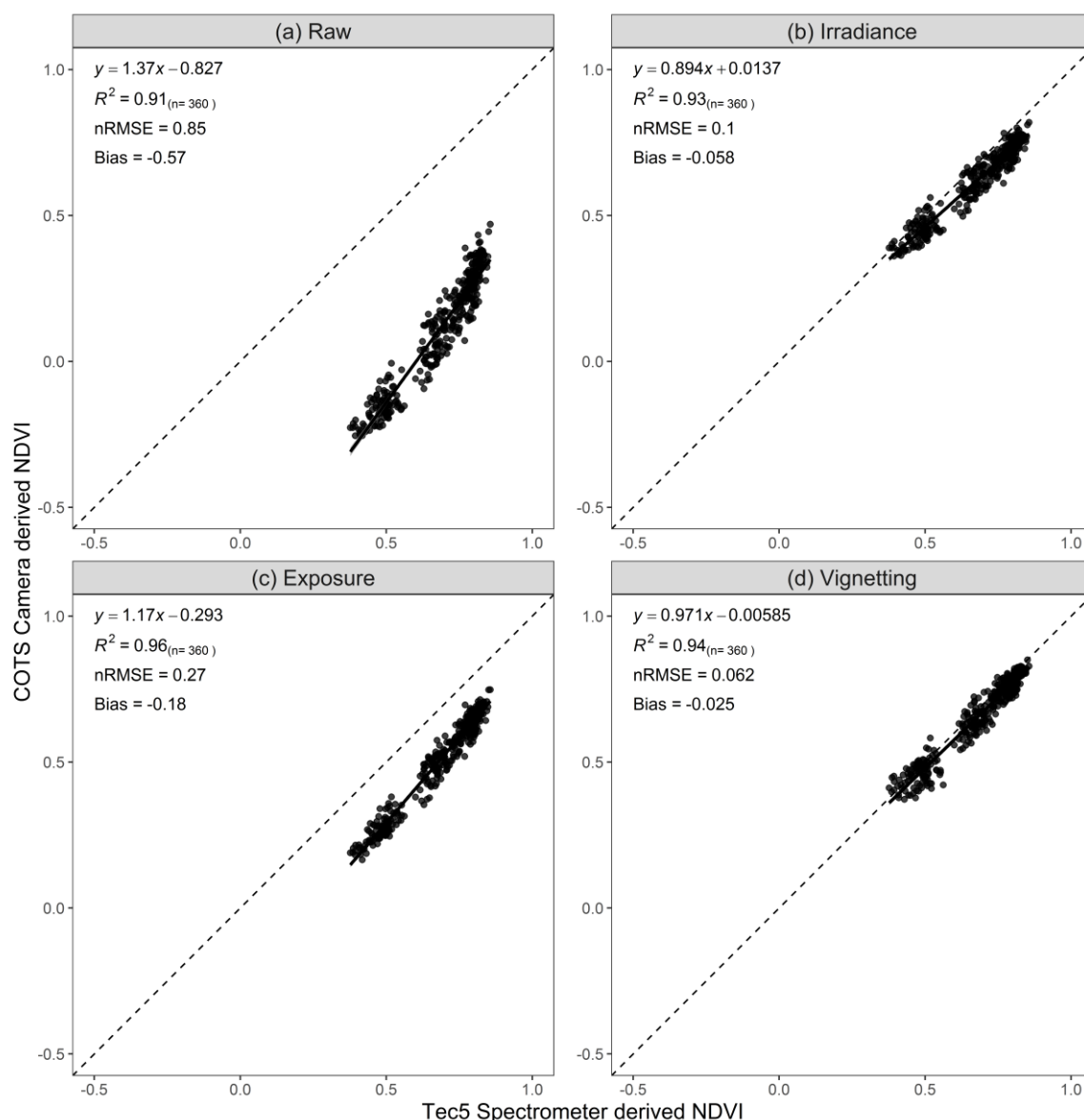
278
279
280
281
282
283
284
285
286

Figure 9. Assessment of the cumulative influence of radiometric corrections applied to COTS camera derived NDVI. Results are compared to COTS camera convolved Tec5 derived NDVI. Dashed line indicates the 1:1 line.

Further investigation of camera settings (Figure 10), *via* calculation on Exposure Value (Equation 7), highlights how the cameras adjusted exposure independently during UAV flight. This independence explains the poor accuracy of NDVI from raw images, where variable camera settings (which can vary between the independent cameras used to gather RGB and NIR data) artificially altering the red to NIR ratio. Inclusion of the varying solar spectral irradiance data corrects this, improving the data consistency greatly; whilst inclusion of exposure and vignetting corrections removes all influence of variable exposure settings, producing even higher accuracy data.

$$ExposureValue_i = 2 \times log_2(f_i) - log_2(t_i) - log_2(ISO_i/100) \qquad (7)$$

Where f_i is the image aperture, t_i is the image shutter speed and ISO_i is the image ISO value.
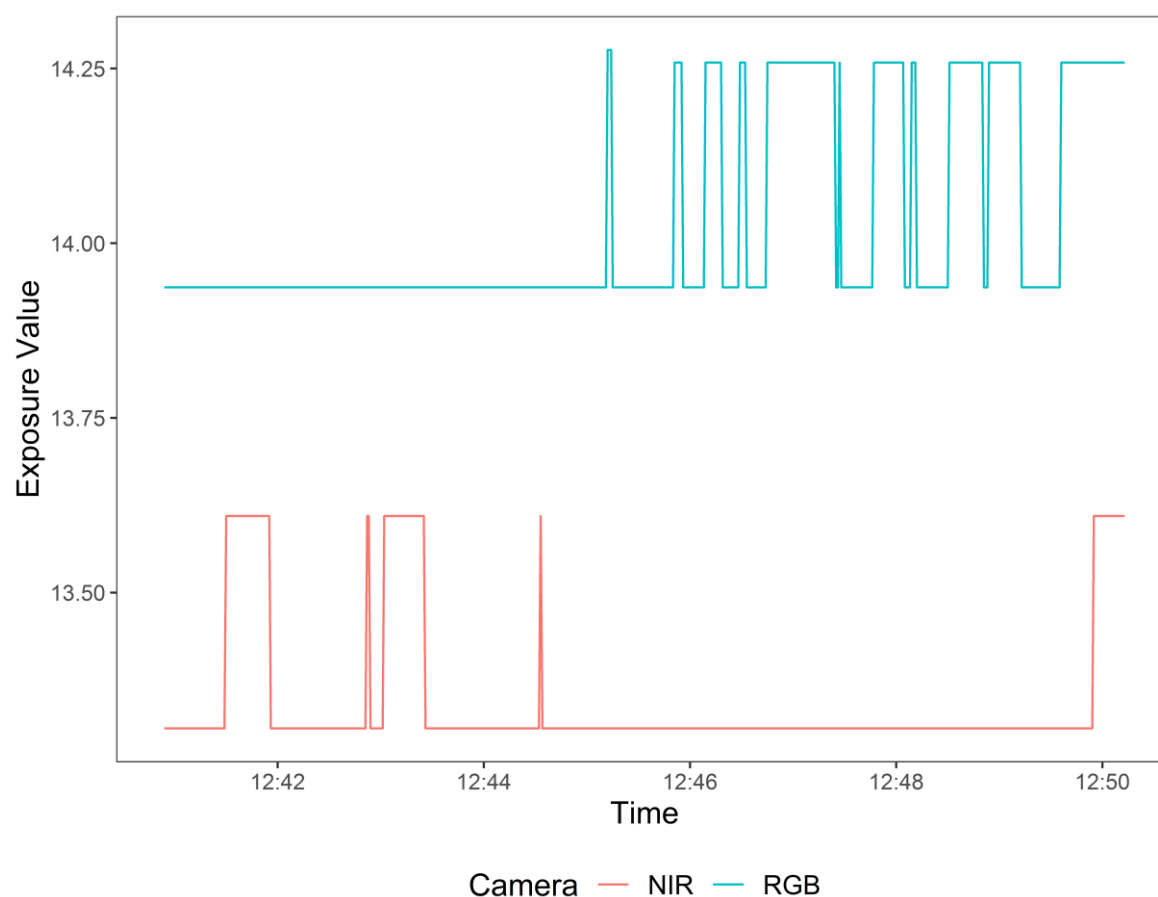
Figure 10. Exposure value for the RGB and NIR cameras over the duration of a flight showing the cameras adjusting erxposure independently. Data is from the flight on 21st June 2017.

3.2 Accuracy Assessment of COTS Camera Reflectance

For three dates (19/04/2017, 21/06/2017, 04/07/2017) COTS camera derived mean plot reflectance and calculated NDVI was assessed against Tec5 results. Poorer results in all statistics in the last date (04/07/17) show reduced agreement with Tec5 reflectance measurements. At this later date, onset of senescence will increase the variability in canopy reflectance both within and between plots, as seen by the increase vertical error bars. This spatial non-uniformity of senescence onset is better measured by the UAV data as opposed to the spectrometer, leading to poorer statistics at this time point.[2]
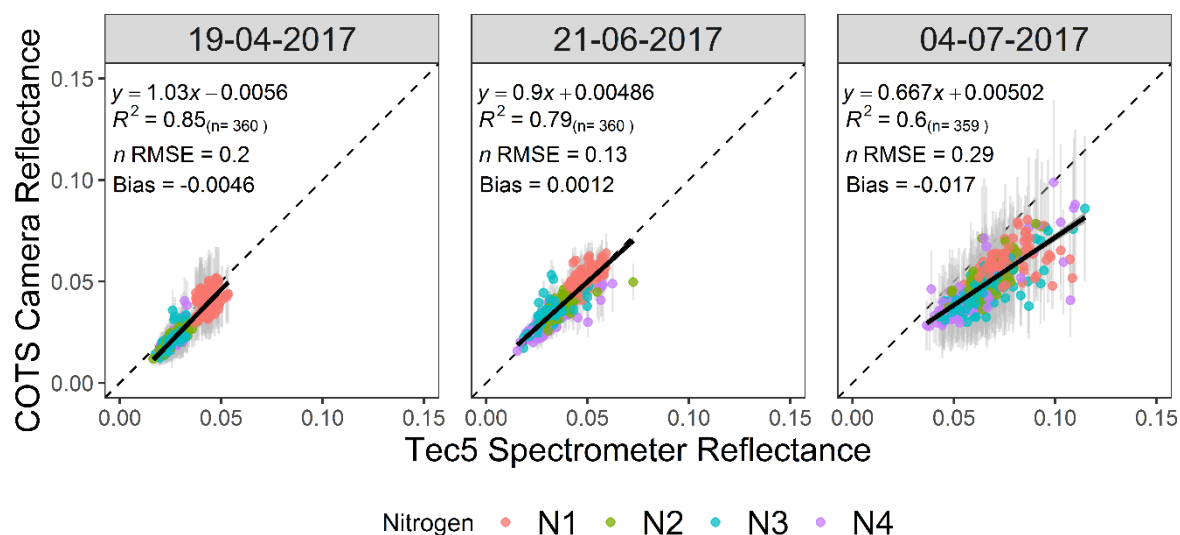
Figure 11. Accuracy assessments of blue band reflectance for three dates. Tec5 reflectance is convolved to the spectral response of the COTS cameras for comparison. The points are coloured based on nitrogen treatment applied to the plot. Standard deviation of reflectance measured by the COTS cameras is presented by vertical error bars. The dashed line represents the 1:1 line.

The green (Figure 12) and red bands (Figure 13) show very similar trends in accuracy to the blue band. Both bands show good fit ($R^2 \geq 0.84$) and consistent small negative biases Bias indicating slight underestimation of reflectance from the cameras. The same trend between nitrogen treatments over time is also present. As well as the greater within plot variation for the last date compared to the earlier two.
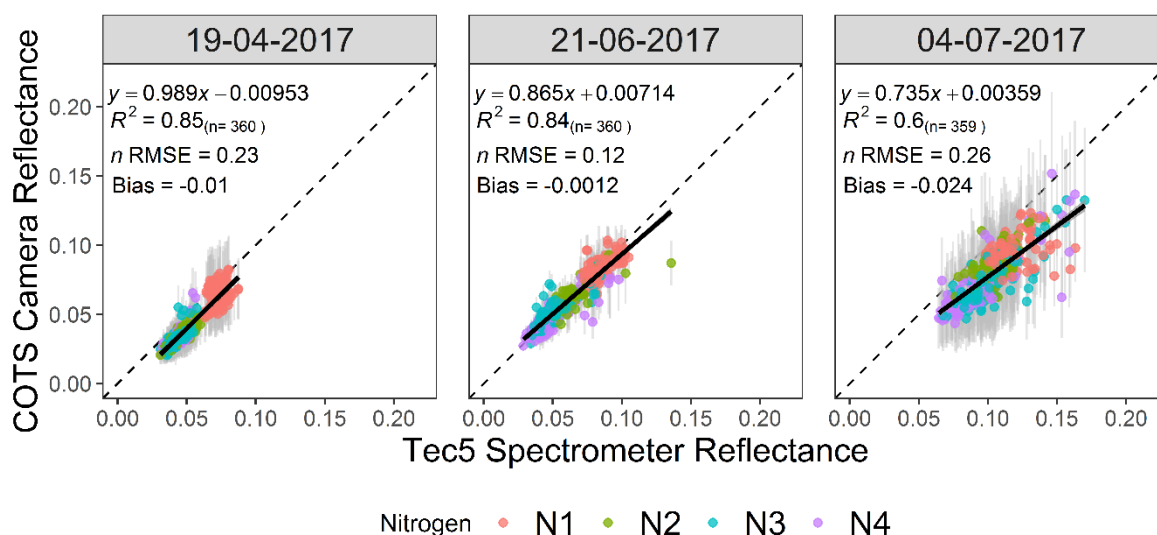

Figure 12. Accuracy assessments of green band reflectance for three dates. Tec5 reflectance is convolved to the spectral response of the COTS cameras for comparison. The points are coloured based on nitrogen treatment applied to the plot. Standard deviation of reflectance measured by the COTS cameras is presented by vertical error bars. The dashed line represents the 1:1 line.
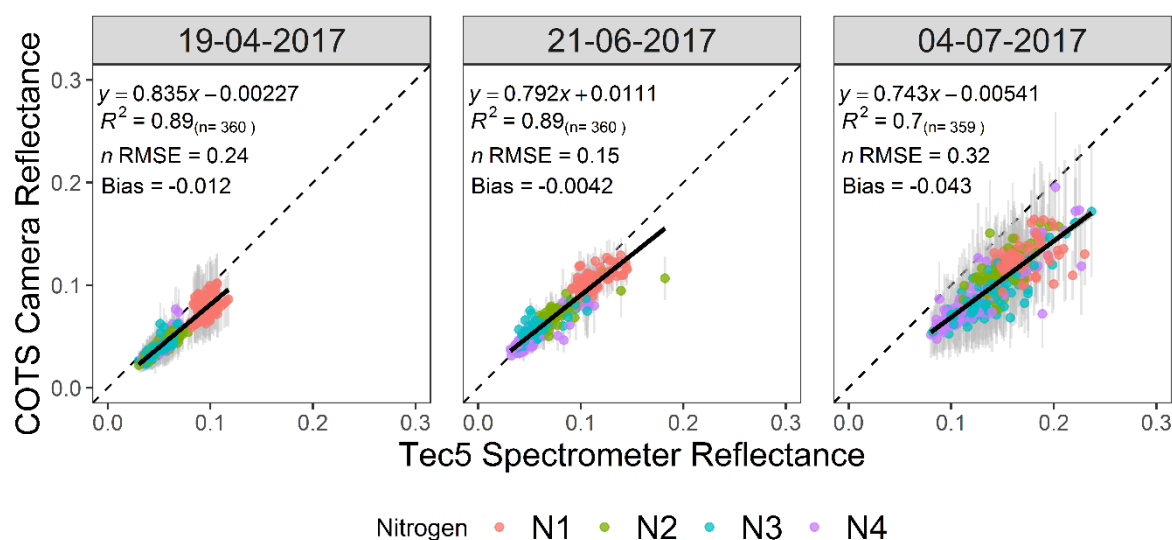
309

Figure 13. Accuracy assessments of red band reflectance for three dates. Tec5 reflectance is convolved to the spectral response of the COTS cameras for comparison. The points are coloured based on nitrogen treatment applied to the plot. Standard deviation of reflectance measured by the COTS cameras is presented by vertical error bars. The dashed line represents the 1:1 line.

310
311   The NIR band (Figure 14) shows reduced fit in comparison to the visible bands ($0.64 \geq R^2 \leq 0.7$)
312 and larger biases indicate lower accuracies achieved in the NIR band. In contrast to the visible bands,
313 the NIR shows lowest accuracy in the first date before improving for the subsequent two dates.
314 Trends between nitrogen treatments shows N1 treatments consistently have lowest reflectance
315 indicating reduced vegetation in these plots as would be expected. Standard deviations show the
316 same increased variability in plot reflectance of the last date. Overall the results of the NIR camera
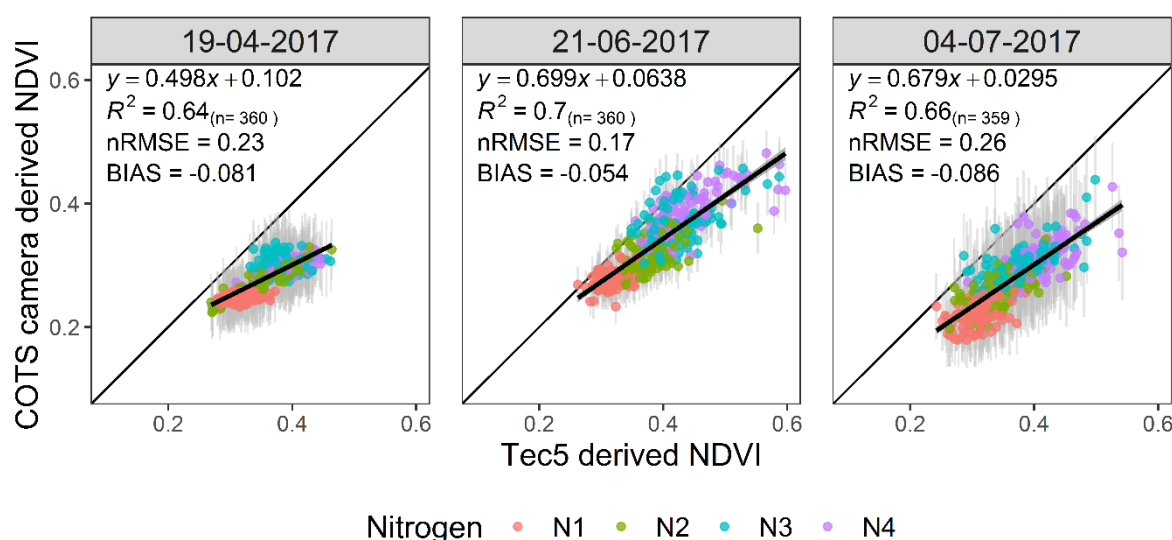317 indicate lower sensitivity to higher canopy reflectance compared to the Tec5.

Figure 14. Accuracy assessments of NIR band reflectance for three dates. Tec5 reflectance is convolved to the spectral response of the COTS cameras for comparison. The points are coloured based on nitrogen treatment applied to the plot. Standard deviation of reflectance measured by the COTS cameras is presented by vertical error bars. The dashed line represents the 1:1 line.

318   Accuracy assessments of calculated NDVI (Figure 15) shows high correlations ($R^2 \geq 0.88$) and
319 low nRMSE and biases indicating overall very good accuracy is achieved from the COTS cameras.
320 Temporal accuracy shows a similar drop in accuracy for the final date as seen in the visible bands,
321 but overall good stability is achieved. The lower accuracy of the NIR band appears to not impact
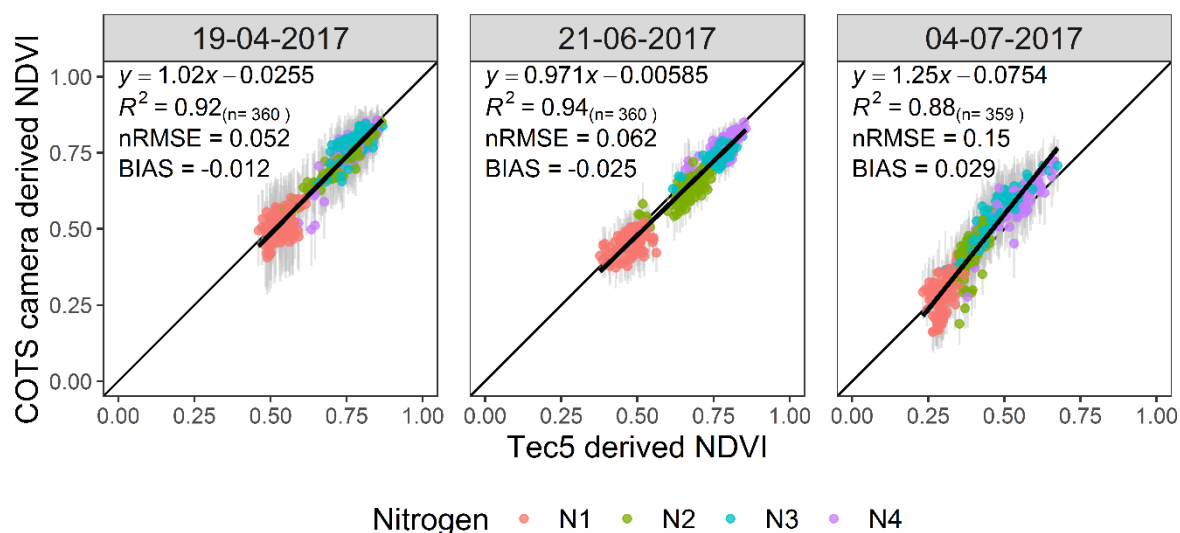322 accuracy of calculated NDVI.

Figure 15. Accuracy assessments COTS camera derived NDVI for three dates. The points are coloured based on nitrogen treatment applied to the plot. Standard deviation of reflectance measured by the COTS cameras is presented by vertical error bars. The dashed line represents the 1:1 line.

323   Additional assessment compared results from the COTS cameras with the Parrot Sequoia
324 (Figure 16), a commercially available multispectral imager whose data is processed using proprietary
325 calibrations. Of the individual bands, green showed the strongest agreement between the two camera
326 systems, with comparable R^2, nRMSE and bias. The red band indicated poorer accuracy achieved by
327 the Sequoia, with large nRMSE, negative biases and poorer linear agreement with the Tec5. In the
328 NIR band, both camera systems showed comparable accuracy levels and precision. NDVI results
329 show greater accuracy achieved by the COTS cameras, with the Sequoia overestimating NDVI
330 compared to the TEC5 (as indicated by positive bias). The similarity in results between the COTS
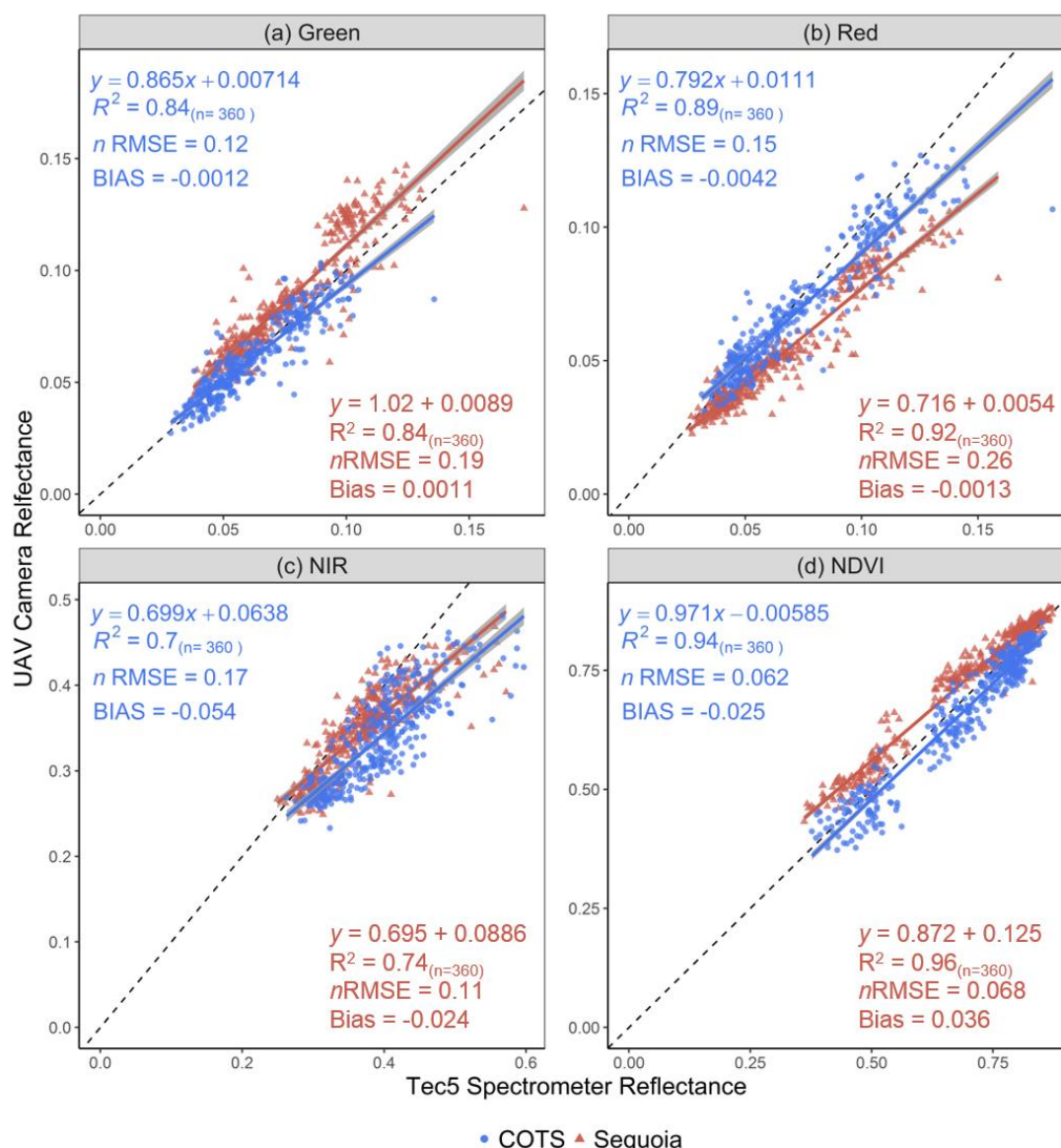331 cameras and Parrot Sequoia, particularly in the NIR waveband, suggests
332

Figure 16. Comparison of accuracies achieved by COTS (blue) cameras and Parrot Sequoia (red) in green, red and NIR reflectance and NDVI. Comparisons are made against Tec5 measure reflectances and NDVI. Reflectance was measured from both cameras on the same date (21/06/2017), whilst the Tec5 was used two days later. The dashed line represents the 1:1 line.

333   *3.3 Influence of canopy on NDVI*

334   The focus of this component of the study was to investigate the potential for high spatial
335   resolution imagery to be used to dissect the influence of canopy cover on derived vegetation indices.
336   For nine dates, the COTS camera imagery was calibrated, processed and NDVI calculated. For one
337   date, 18/05/2017, significant shadowing impacted on results of masking; as such this date was
338   removed from further processing. For the remaining eight dates, a subset of ten varieties have been
339   used. Examples of NDVI orthomosaic crops for three dates highlight the temporal and spatial
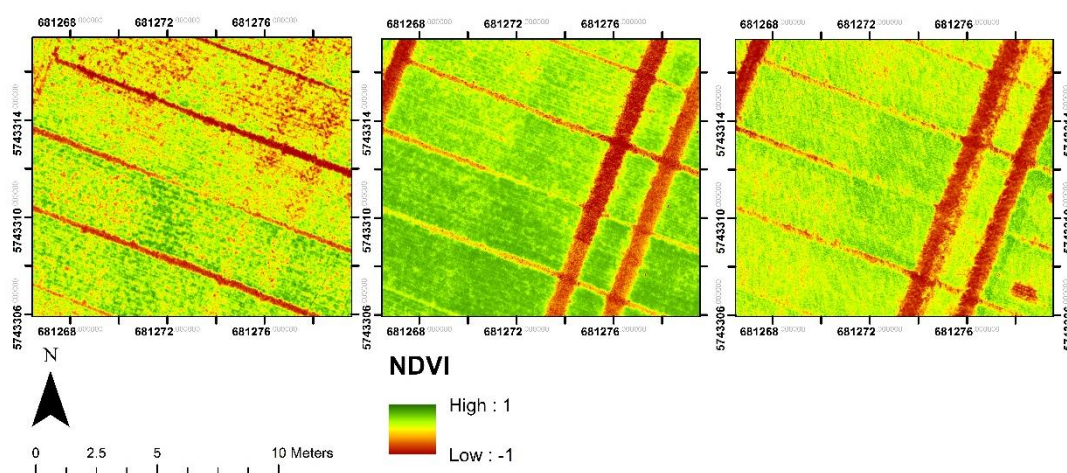340   variation achieved from the COTS cameras (Figure 17).

Figure 17. Example subset of NDVI orthomosaics from three dates - 27/03/2017 (left), 18/05/2017 (middle), 21/06/2017 (right). Orthomosaics highlight the spatial variability of NDVI both between and within plots.

341   Assessment of NDVI$_{unmasked}$ (Figure 18(a), top row) show typical trends over time and between
342   nitrogen treatments. All varieties and treatment levels show a starting NDVI value around 0.4,
343   increasing to a peak in late-May before dropping off at the end of the season. Comparison between
344   nitrogen treatments shows clear differences between plots with (N2, N3 and N4) and without (N1)
345   fertiliser application, with the N1 treatment showing lower maximum NDVI, despite similar initial
346   NDVI values (~0.4). The drop in NDVI values at the end of the season is likely a result of senescence
347   and the browning of crop canopy. Application of ExGR derived masks (Figure 18(b), second row) to
348   extract NDVI of green classified pixels only, produces new trends between treatments and over time.
349   For all treatments, shallower temporal trends in NDVI are observed, with the N1 treatment
350   displaying a close to horizontal trend with the peak in late-May no longer featuring. Comparing the
351   difference between NDVI$_{unmasked}$ and NDVI$_{ExGR}$ (Figure 18(c), third row) shows the greatest influence
352   of masking occurs early season where % green pixel is lowest (Figure 18(d), bottom row).
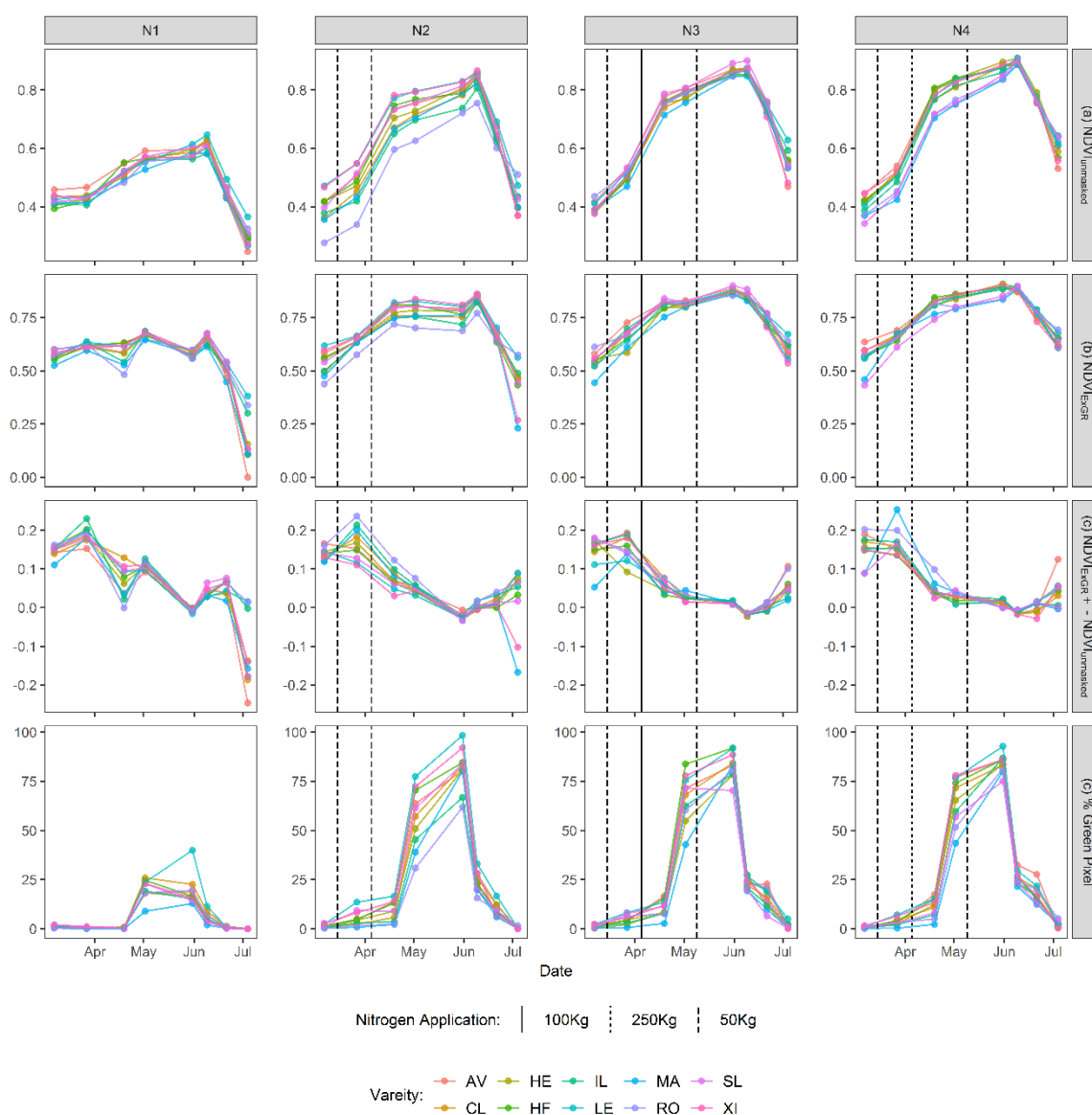
Figure 18. Temporal trends of ten wheat varieties grown under four different nitrogen treatments for: (a) the standard unmasked mean NDVI; (b) mean NDVI derived from ExGR masked plots to remove the influence of background soil; (c) displaying temporal differences between masked and unmasked NDVI results; (d) percentage green pixel as calculated from the ExGR masks. Nitrogen application dates and quantities for the N2, N3 and N4 treatments are presented by the vertical lines. All data represent the means of three replicates.

4. Discussion

This study has provided a quantitative assessment of commercial off the shelf (COTS) digital cameras for supporting the UAV-based remote sensing of field-based crop trials. COTS cameras provide very high spatial resolution imagery, potentially enabling the separation of canopy influences on vegetation indices from those of the background soil and thus making the derived information more relevant to crop health assessment and monitoring.

We have designed and tested a data processing workflow to radiometrically calibrate COTS camera imagery into reflectance units, in blue, green, red and NIR wavebands. Cameras were allowed to vary their exposure settings during flight, to cope with varying solar illumination conditions, whilst having a fixed shutter speed to avoid blurring from the UAV-motion. We find that our

363 processing workflow can cope with this setup, and that the influence of the different pre-processing
364 steps varies by band. In particular, the NIR band showed greater impact from vignetting corrections
365 than the visible wavebands, agreeing with past studies who found the modified internal filters used
366 in NIR COTS cameras increases the impact of vignetting in images by up to 30% [16,25]. The influence
367 of varied exposure settings as well as the success of the developed corrections was perhaps most clear
368 during calculations of NDVI, because the separate visible and NIR COTS cameras used did not
369 necessarily change their exposure settings in the same way at the same time, leading to artificial
370 changes in derived NDVI. Even without corrections, good precision is seen for the NDVI metrics
371 calculated, with trends in NDVI cross between plots maintained. However, NDVI values calculated
372 from such raw camera data (or that calibrated into radiances rather than reflectances) are always
373 significantly different to those derived from calibrated reflectances, and this difference is sensor
374 specific [41]. Ultimately this means VIs calculated from different sensors can be only be
375 intercompared in a fully meaningful way if calculated from calibrated reflectance measures.

376 Temporal consistency of the developed workflow was tested over three dates *via* comparison of
377 COTS camera and Tec5 field-spectrometer derived mean plot reflectance. Results showed good
378 accuracy with NDVI results ($R^2 \geq 0.88$, nRMSE ≤ 0.15) comparable to those achieved by other studies
379 [25,42,43]. Consistency of results over this period indicates a good level of robustness in the
380 developed methods for variable weather conditions both during and between data collection flights.
381 Some variability occurred between time points in all bands and NDVI; likely a result of the UAV and
382 Tec5 spectrometer obtaining measurements at different spatial resolutions [38] and datasets not being
383 collected on the same date. Rossi *et al.* [44] demonstrated the impact of non-concurrent data collection
384 when comparing different reflectance from different sensors, with a single day lag negatively
385 impacting on correlation results. Variability in accuracy also occurred between bands, particularly
386 for visible *vs.* NIR, which was observed consistently over time. The same variations were also
387 observed in the Parrot Sequoia results, as well as by Aasen and Bolten [38], who found the varying
388 field of views between cameras and spectrometers coupled with varying bidirectional reflectance
389 factors in visible and NIR wavelengths impacted on correlations in the NIR band. Lack of influence
390 of the NIR results on NDVI accuracy further indicates disparity between imaging and non-imaging
391 measurement systems, as opposed to error in the NIR band. Investigation of this variability between
392 bands and data sources should be a focus of future work.

393 Application of the very high resolution (GSD = 1cm) reflectance imagery over time was used to
394 investigate the impact of canopy cover and background soil on derived NDVI. Results of the
395 unmasked NDVI presented temporal trends over a season in relation to differing nitrogen treatments
396 and for different wheat varieties. Masking of background soil pixels, *via* Excess Green Red, offered
397 new insights into temporal NDVI trends in relation to canopy cover. Greatest differences between
398 $NDVI_{unmasked}$ and $NDVI_{ExGR}$ (Figure 18 (d)) occurred in the early season, where canopy cover is lowest
399 [45], indicating background soil and canopy cover can artificially influence measured vegetation
400 indices. Isolation of the crop canopy for VI measurements should provide improved relationships
401 between VI and traits of interest such as yield, canopy quality, senescence and canopy chlorophyll
402 content [10,46], and therefore should be a focus of future studies.

403 ## 5. Conclusion

404 This study has presented methods for radiometric calibration of commercial off the shelf digital
405 camera imagery to reflectance for use in plant phenotyping. New calibrations for image exposure
406 normalisation, combined with robust vignetting and irradiance corrections produced accurate
407 reflectance and NDVI, comparable to a Parrot Sequoia multispectral camera and Tec5 ground
408 spectrometer. The very high-resolution imagery obtained provided new insights into the influence
409 of canopy cover and background soil on derived plot NDVI, especially in the early season. Future
410 studies should look to incorporate additional UAV phenotyping methods such as 3D structure and
411 thermal measurements to provide a more extensive low-cost phenotyping UAV based system.

Conflicts of Interest: The authors declare no conflict of interest.

6. References

1. *Physiological breeding II: a field guide to wheat phenotyping*; Pask, A.J.D., Pietragalla, J., Mullan, D.M., Reynolds, M.P., Eds.; CIMMYT, 2012;

2. Khan, Z.; Chopin, J.; Cai, J.; Eichi, V.-R.; Haefele, S.; Miklavcic, S.; Khan, Z.; Chopin, J.; Cai, J.; Eichi, V.-R.; et al. Quantitative Estimation of Wheat Phenotyping Traits Using Ground and Aerial Imagery. *Remote Sensing* **2018**, *10*, 950.

3. Kipp, S.; Mistele, B.; Baresel, P.; Schmidhalter, U. High-throughput phenotyping early plant vigour of winter wheat. *European Journal of Agronomy* **2014**, *52*, 271–278.

4. Cabrera-Bosquet, L.; Molero, G.; Stellacci, A.M.; Bort, J.; Nogués, S.; Araus, J.L. NDVI as a Potential Tool for Predicting Biomass, Plant Nitrogen Content and Growth in Wheat Genotypes Subjected to Different Water and Nitrogen Conditions. *Cereal Research Communications* **2011**, *39*, 147–159.

5. Bendig, J.; Bolten, A.; Bennertz, S.; Broscheit, J.; Eichfuss, S.; Bareth, G. Estimating Biomass of Barley Using Crop Surface Models (CSMs) Derived from UAV-Based RGB Imaging. *Remote Sensing* **2014**, *6*, 10395–10412.

6. Muñoz-Huerta, R.F.; Guevara-Gonzalez, R.G.; Contreras-Medina, L.M.; Torres-Pacheco, I.; Prado-Olivarez, J.; Ocampo-Velazquez, R.V. A Review of Methods for Sensing the Nitrogen Status in Plants: Advantages, Disadvantages and Recent Advances. *Sensors (Basel)* **2013**, *13*, 10823–10843.

7. Ali, M.; Montzka, C.; Stadler, A.; Menz, G.; Thonfeld, F.; Vereecken, H.; Ali, M.; Montzka, C.; Stadler, A.; Menz, G.; et al. Estimation and Validation of RapidEye-Based Time-Series of Leaf Area Index for Winter Wheat in the Rur Catchment (Germany). *Remote Sensing* **2015**, *7*, 2808–2831.

8. Zheng, G.; Moskal, L.M.; Zheng, G.; Moskal, L.M. Retrieving Leaf Area Index (LAI) Using Remote Sensing: Theories, Methods and Sensors. *Sensors* **2009**, *9*, 2719–2745.

9. Lopresti, M.F.; Di Bella, C.M.; Degioanni, A.J. Relationship between MODIS-NDVI data and wheat yield: A case study in Northern Buenos Aires province, Argentina. *Information Processing in Agriculture* **2015**, *2*, 73–84.

10. Jay, S.; Gorretta, N.; Morel, J.; Maupas, F.; Bendoula, R.; Rabatel, G.; Dutartre, D.; Comar, A.; Baret, F. Estimating leaf chlorophyll content in sugar beet canopies using

millimeter- to centimeter-scale reflectance imagery. *Remote Sensing of Environment* **2017**, *198*, 173–186.

11. Duan, T. Dynamic monitoring of NDVI in wheat agronomy and breeding trials using an unmanned aerial vehicle. *Field crops research* **2017**, *v. 210*, 71–80.

12. Holman, F.H.; Riche, A.B.; Michalski, A.; Castle, M.; Wooster, M.J.; Hawkesford, M.J. High Throughput Field Phenotyping of Wheat Plant Height and Growth Rate in Field Plot Trials Using UAV Based Remote Sensing. *Remote Sensing* **2016**, *8*, 1031.

13. Parrot SEQUOIA+ | Parrot Store Official Available online: https://www.parrot.com/business-solutions-uk/parrot-professional/parrot-sequoia (accessed on Apr 8, 2019).

14. Young, N.E.; Anderson, R.S.; Chignell, S.M.; Vorster, A.G.; Lawrence, R.; Evangelista, P.H. A survival guide to Landsat preprocessing. *Ecology* **2017**, *98*, 920–932.

15. Lebourgeois, V.; Bégué, A.; Labbé, S.; Mallavan, B.; Prévot, L.; Roux, B. Can Commercial Digital Cameras Be Used as Multispectral Sensors? A Crop Monitoring Test. *Sensors* **2008**, *8*, 7300–7322.

16. Lelong, C.C.D.; Burger, P.; Jubelin, G.; Roux, B.; Labbé, S.; Baret, F. Assessment of Unmanned Aerial Vehicles Imagery for Quantitative Monitoring of Wheat Crop in Small Plots. *Sensors (Basel)* **2008**, *8*, 3557–3585.

17. Mathews, A.J. A Practical UAV Remote Sensing Methodology to Generate Multispectral Orthophotos for Vineyards: Estimation of Spectral Reflectance Using Compact Digital Cameras. *International Journal of Applied Geospatial Research* **2015**, *6*, 65–87.

18. Gibson-Poole, S.; Humphris, S.; Toth, I.; Hamilton, A. Identification of the onset of disease within a potato crop using a UAV equipped with un-modified and modified commercial off-the-shelf digital cameras. *Advances in Animal Biosciences* **2017**, *8*, 812–816.

19. Filippa, G.; Cremonese, E.; Migliavacca, M.; Galvagno, M.; Sonnentag, O.; Humphreys, E.; Hufkens, K.; Ryu, Y.; Verfaillie, J.; Morra di Cella, U.; et al. NDVI derived from near-infrared-enabled digital cameras: Applicability across different plant functional types. *Agricultural and Forest Meteorology* **2018**, *249*, 275–285.

20. Petach, A.R.; Toomey, M.; Aubrecht, D.M.; Richardson, A.D. Monitoring vegetation phenology using an infrared-enabled security camera. *Agricultural and Forest Meteorology* **2014**, *195–196*, 143–151.

21. Sakamoto, T.; Shibayama, M.; Kimura, A.; Takada, E. Assessment of digital camera-derived vegetation indices in quantitative monitoring of seasonal rice growth. *ISPRS Journal of Photogrammetry and Remote Sensing* **2011**, *66*, 872–882.

22. Sakamoto, T.; Gitelson, A.A.; Nguy-Robertson, A.L.; Arkebauer, T.J.; Wardlow, B.D.; Suyker, A.E.; Verma, S.B.; Shibayama, M. An alternative method using digital cameras for continuous monitoring of crop status. *Agricultural and Forest Meteorology* **2012**, *154–155*, 113–126.

23. Luo, Y.; El-Madany, T.S.; Filippa, G.; Ma, X.; Ahrens, B.; Carrara, A.; Gonzalez-Cascon, R.; Cremonese, E.; Galvagno, M.; Hammer, T.W.; et al. Using Near-Infrared-

Enabled Digital Repeat Photography to Track Structural and Physiological Phenology in Mediterranean Tree–Grass Ecosystems. *Remote Sensing* **2018**, *10*, 1293.

24. Kelcey, J.; Lucieer, A. Sensor Correction of a 6-Band Multispectral Imaging Sensor for UAV Remote Sensing. *Remote Sensing* **2012**, *4*, 1462–1493.

25. Berra, E.F.; Gaulton, R.; Barr, S. Commercial Off-the-Shelf Digital Cameras on Unmanned Aerial Vehicles for Multitemporal Monitoring of Vegetation Reflectance and NDVI. *IEEE Transactions on Geoscience and Remote Sensing* **2017**, *55*, 4878–4886.

26. Smith, G.M.; Milton, E.J. The use of the empirical line method to calibrate remotely sensed data to reflectance. *International Journal of Remote Sensing* **1999**, *20*, 2653–2662.

27. Anderson, K.; Milton, E.J. Characterisation of the apparent reflectance of a concrete. **2005**.

28. G. L. Ritchie; D. G. Sullivan; C. D. Perry; J. E. Hook; C. W. Bednarz Preparation of a Low-Cost Digital Camera System for Remote Sensing. *Applied Engineering in Agriculture* **2008**, *24*, 885–894.

29. Hiscocks, P.D. Measuring Luminance with a digital camera. *Syscomp Electronic Design Limited* **2011**.

30. Spreading Wings S900 - highly portable, powerful aerial system for the demanding filmmaker Available online: https://www.dji.com/uk/spreading-wings-s900 (accessed on Apr 8, 2019).

31. Smart Camera | a5100 NFC & Wi-Fi Enabled Digital Camera | Sony UK Available online: https://www.sony.co.uk/electronics/interchangeable-lens-cameras/ilce-5100-body-kit (accessed on Apr 8, 2019).

32. Berra, E.; Gibson-Poole, S.; MacArthur, A.; Gaulton, R.; Hamilton, A. ESTIMATION OF THE SPECTRAL SENSITIVITY FUNCTIONS OF UN-MODIFIED AND MODIFIED COMMERCIAL OFF-THE-SHELF DIGITAL CAMERAS TO ENABLE THEIR USE AS A MULTISPECTRAL IMAGING SYSTEM FOR UAVS. *ISPRS - International Archives of the Photogrammetry, Remote Sensing and Spatial Information Sciences* **2015**, *XL-1/W4*, 207–214.

33. Geo 7X | Handhelds | Trimble Geospatial Available online: https://geospatial.trimble.com/products-and-solutions/geo-7x (accessed on Apr 8, 2019).

34. Customized Systems for HandySpec® Field | tec5 Available online: https://www.tec5.com/en/products/custom-solutions/handyspec-field (accessed on Apr 8, 2019).

35. Professional photogrammetry and drone mapping software Available online: https://www.pix4d.com/ (accessed on Apr 10, 2019).

36. Decoding raw digital photos in Linux Available online: https://www.cybercom.net/~dcoffin/dcraw/ (accessed on Feb 18, 2019).

37. Agisoft Agisoft PhotoScan User Manual Professional Edition, Version 1.2 2016.

538   38.   Aasen, H.; Bolten, A. Multi-temporal high-resolution imaging spectroscopy with
539   hyperspectral 2D imagers – From theory to application. *Remote Sensing of Environment*
540   **2018**, *205*, 374–389.
541   39.   Meyer, G.E.; Neto, J.C. Verification of color vegetation indices for automated crop
542   imaging applications. *Computers and Electronics in Agriculture* **2008**, *63*, 282–293.
543   40.   Sadeghi-Tehran, P.; Virlet, N.; Sabermanesh, K.; Hawkesford, M.J. Multi-feature
544   machine learning model for automatic segmentation of green fractional vegetation cover
545   for high-throughput field phenotyping. *Plant Methods* **2017**, *13*, 103.
546   41.   Zhou, X.; Guan∗∗, H.; Xie, H.; Wilson, J.L. Analysis and optimization of NDVI
547   definitions and areal fraction models in remote sensing of vegetation. *International*
548   *Journal of Remote Sensing* **2009**, *30*, 721–751.
549   42.   Hassan, M.A.; Yang, M.; Rasheed, A.; Jin, X.; Xia, X.; Xiao, Y.; He, Z. Time-Series
550   Multispectral Indices from Unmanned Aerial Vehicle Imagery Reveal Senescence Rate
551   in Bread Wheat. *Remote Sensing* **2018**, *10*, 809.
552   43.   Hassan, M.A.; Yang, M.; Rasheed, A.; Yang, G.; Reynolds, M.; Xia, X.; Xiao, Y.; He,
553   Z. A rapid monitoring of NDVI across the wheat growth cycle for grain yield prediction
554   using a multi-spectral UAV platform. *Plant Science* **2019**, *282*, 95–103.
555   44.   Rossi, M.; Niedrist, G.; Asam, S.; Tonon, G.; Tomelleri, E.; Zebisch, M. A Comparison
556   of the Signal from Diverse Optical Sensors for Monitoring Alpine Grassland Dynamics.
557   *Remote Sensing* **2019**, *11*, 296.
558   45.   Agriculture and Horticulture Development Board *Wheat Growth Guide*; AHDB:
559   Warwickshire, 2015;
560   46.   Makanza, R.; Zaman-Allah, M.; Cairns, J.; Magorokosho, C.; Tarekegne, A.; Olsen,
561   M.; Prasanna, B.; Makanza, R.; Zaman-Allah, M.; Cairns, J.E.; et al. High-Throughput
562   Phenotyping of Canopy Cover and Senescence in Maize Field Trials Using Aerial
563   Digital Canopy Imaging. *Remote Sensing* **2018**, *10*, 330.
564
565